

# Analogue switches made from boron nitride monolayers for application in 5G and terahertz communication systems

Myungsoo Kim<sup>®</sup>¹, Emiliano Pallecchi<sup>®</sup>², Ruijing Ge¹, Xiaohan Wu<sup>®</sup>¹, Guillaume Ducournau², Jack C. Lee¹, Henri Happy<sup>®</sup>² and Deii Akinwande<sup>®</sup>¹™

Hexagonal boron nitride (hBN) has a large bandgap, high phonon energies and an atomically smooth surface absent of dangling bonds. As a result, it has been widely used as a dielectric to investigate electron physics in two-dimensional heterostructures and as a dielectric in the fabrication of two-dimensional transistors and optoelectronic devices. Here we show that hBN can be used to create analogue switches for applications in communication systems across radio, 5G and terahertz frequencies. Our approach relies on the non-volatile resistive switching capabilities of atomically thin hBN. The switches are composed of monolayer hBN sandwiched between two gold electrodes and exhibit a cutoff-frequency figure of merit of around 129 THz with a low insertion loss ( $\leq$ 0.5 dB) and high isolation ( $\geq$ 10 dB) from 0.1 to 200 GHz, as well as a high power handling (around 20 dBm) and nanosecond switching speeds, metrics that are superior to those of existing solid-state switches. Furthermore, the switches are 50 times more efficient than other non-volatile switches in terms of a d.c. energy-consumption metric, which is an important consideration for ubiquitous mobile systems. We also illustrate the potential of the hBN switches in a communication system with an 8.5 Gbit  $\rm s^{-1}$  data transmission rate at 100 GHz with a low bit error rate under  $\rm 10^{-10}$ .

nalogue switches are used in communication and connectivity systems to switch between different frequency bands, route signals between transmit and receive antennas, reconfigure wireless communication systems and form directional beams in phased-array networks<sup>1-12</sup>. Conventional analogue and radio-frequency (RF) switches are based on solid-state diode or transistor devices<sup>2,3,6</sup>, which are volatile and consume energy both during the relatively long static (standby) and short dynamic (switching) periods. Thus, there is interest in developing switches that approach the ideal operation of zero d.c. power consumption, with finite energy only during a switching event. This is of particular importance in mobile, wearable and battery-operated wireless systems.

To develop such an ideal switch, non-volatile memory devices, which include memristors, resistive random-access memory and phase-change memory, have been investigated intensely<sup>1,8–11,13–19</sup>. The primary requirements of a memory device for high-frequency switching are a low on-state resistance ( $R_{\rm on}$  « 50  $\Omega$ ) to afford a low insertion loss, and a low off-state capacitance ( $C_{\rm off}$ ) to enable high isolation. Both parameters combine to yield a single cutoff frequency ( $F_{\rm CO}=1/2\pi R_{\rm on}C_{\rm off}$ ) figure of merit in the terahertz range that is used to benchmark candidate switches<sup>1,9,17</sup>. Additional metrics of practical importance include switching voltage, operation bandwidth, signal-power handling and switching time.

In this article, we show that atomically thin sheets of hexagonal boron nitride (hBN) configured in a metal–insulator–metal (MIM)<sup>20–22</sup> sandwich on a diamond substrate can be used as analogue switches with a state-of-the-art performance with respect to the  $F_{\rm CO}$  (129 THz), bandwidth above 200 GHz, switching time and area scalability. In addition, we define a d.c. energy consumption per switching event figure of merit,  $E_{\rm FOM} = V_{\rm set} I_{\rm on} \tau$ , where  $V_{\rm set}$  is the

set voltage (~0.9 V),  $I_{\rm on}$  is the on current or maximum compliance current (~50 mA) and  $\tau$  is the switching time (<15 ns). This metric is a useful estimate for benchmarking the energy efficiency of candidate switches for modern mobile systems, which are generally energy constrained. By this metric, our hBN switch ( $E_{\rm FOM}$  < 0.68 nJ) is more energy efficient than conventional emerging switching devices by a factor of about 50 or more<sup>8,15,19</sup>.

The high-speed data-transmission quality of our hBN switches is validated using eye-diagram and bit error rate (BER) measurements for an 8.5 Gbit s<sup>-1</sup> data stream at a carrier frequency  $(f_c)$  of 100 GHz. This data rate, although limited by the experimental set-up, is more than sufficient to meet the specified user experience data rate for 5G of 100 Mbit s<sup>-1</sup> (ref. <sup>23</sup>). The intrinsic data rate, which is dependent on the hBN operational bandwidth (>200 GHz), is similarly sufficient to satisfy the required peak data rate of 20 Gbit s<sup>-1</sup>. Compared with monolayer MoS<sub>2</sub> switches, which have a similar MIM configuration<sup>24</sup>, hBN switches offer ten times more power handling due to their superior thermomechanical properties. To further increase the thermal reliability and potentially higher power handling, optimized thermal management is required to overcome Joule heating—a leading cause of device failure. To this end, we also used multiphysics simulation to model the electrothermal performance and develop a route to optimize material and device co-design.

**Structure, characterization and d.c. resistive switching.** Figure 1 shows the device structure and optical characterization of a monolayer hBN RF switch fabricated on a 300- $\mu$ m-thick polycrystalline diamond substrate that has a root-mean-square surface roughness less than 0.8 nm (Supplementary Fig. 1). In comparison with silicon or SiO<sub>2</sub>/silicon substrates, the diamond was specifically chosen for its high thermal conductivity, which provides sufficient heat sinking to

ARTICLES NATURE ELECTRONICS

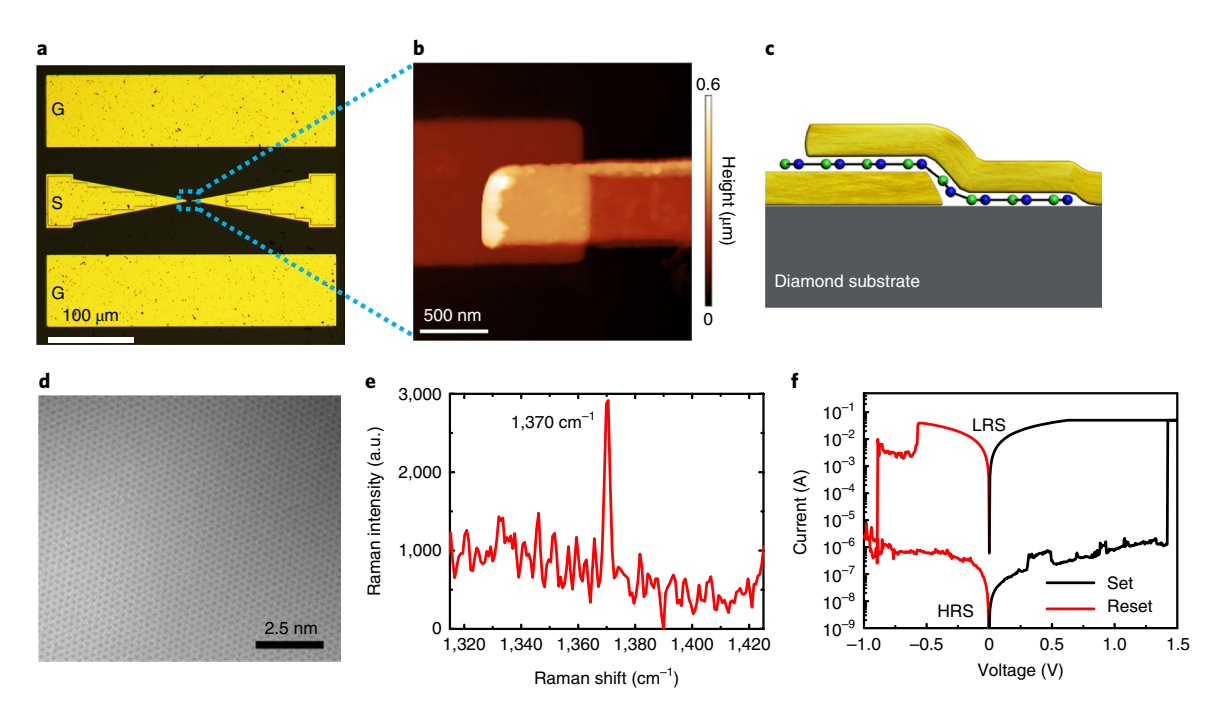


**Fig. 1 | Device structure and material characterization. a**, Optical microscopy image of a fabricated monolayer hBN RF switch with GSG Au electrodes. The dashed box in **a** marks the area in which the vertical MIM structure is located. **b**, Representative atomic force microscopy image of the dashed box region in **a** with an overlap area of  $0.5 \times 0.5 \, \mu m^2$ . **c**, Simplified side-view illustration of the RF switch device on a diamond substrate. **d**, Atomic-resolution transmission electron microscopy image of CVD-grown hBN. **e**, Raman spectroscopy of CVD-grown monolayer hBN. **f**, Typical current-voltage curve of the resistive switching behaviour of a monolayer hBN device with an overlap area of  $0.5 \times 0.5 \, \mu m^2$ . HRS, high-resistance state; LRS, low-resistance state.

keep the hBN switch (and metal feedlines) relatively cool during d.c. and RF operation (Supplementary Fig. 2), an important criterion for reliable operation. The switch stack consists of ~150 nm gold (Au) top and bottom electrodes (TEs and BEs, respectively) both with 2 nm chromium adhesion layers. First, BEs with a ground-signalground (GSG) configuration for RF measurements were formed by lift-off after electron-beam lithography and electron-beam metal evaporation. Afterwards, chemical vapour deposited (CVD) hBN atomic sheets were transferred onto the BE using poly(methyl methacrylate)-assisted wet transfer methods<sup>20,25</sup>. The TE was prepared using the same fabrication process as for the BE. Figure 1a shows a top-view optical image of a GSG device configuration of an hBN RF switch with Au electrodes. Figure 1b is a magnified atomic force microscopy image of the device area of a vertical MIM structure. The overlap between the BE and TE defines the switch area, which in this case is  $0.5 \times 0.5 \,\mu\text{m}^2$ . A side-view schematic of the device MIM structure is shown in Fig. 1c. Transmission electron microscopy confirms the crystalline honeycomb atomic structure of the synthesized monolayer hBN with a lattice constant of ~0.25 nm (Fig. 1d). Furthermore, Raman spectroscopy of the CVD-grown hBN film corroborates the crystalline quality (Fig. 1e). After fabrication, the device is initially in a high-resistance state (HRS). Electrical voltage stimulus reveals a sudden increase (set process) in the current (Fig. 1f), which corresponds to a low-resistance state. It remains in that state, absent of power, until an opposite voltage polarity is employed to reset the device back to its initial state. As such, this type of MIM device is known as a bipolar non-volatile resistance switch or memory device<sup>13</sup>.

**High-frequency performance studies.** High-frequency scattering (S)-parameter measurements were conducted in both the on and off states of the hBN switch using a vector network analyser (VNA). At the outset, as is standard practice, SOLT (short-open-load-through) or LRRM (line-reflect-reflect-match) on-wafer calibrations were

performed to obtain precise results and to remove the extrinsic effects of the test cables and probe station<sup>26</sup>. Subsequently, de-embedding processes using test patterns fabricated on the same substrate were conducted to obtain the intrinsic S parameters of hBN RF switches by eliminating the probe-pad and interconnect resistances<sup>26</sup>. The intrinsic experimental high-frequency characteristics of the monolayer hBN switch show ~0.27 dB insertion loss in the on state (Fig. 2a) and isolation below 35 dB in the off state (Fig. 2b) at frequencies up to 67 GHz. The three performance parameters,  $R_{on}$ ,  $C_{\rm off}$  and  $F_{\rm CO}$  (refs. <sup>1,27</sup>), were determined using an equivalent lumped element circuit model (Supplementary Fig. 3 and Supplementary Note 1). After the de-embedding process,  $R_{on}$  and  $C_{off}$  were extracted from the intrinsic S parameters in the on and off states, respectively, to obtain their quasi-static values. The  $F_{CO}$  was calculated to be ~129 THz. These hBN switch results, although at a nascent state, outperform the phase-change memory, memristive and microelectromechanical system RF switches with the added benefit of a heater-less ambient integration (Supplementary Table 1)<sup>24</sup>. Another point of comparison is the switching ratio,  $S_{21,off} - S_{21,on}$ , with hBN clearly showing a higher ratio compared with those of other emerging RF switch devices (Supplementary Fig. 4).

A noteworthy observation is the decreasing insertion loss of the hBN switch with frequency, a beneficial feature in contrast to conventional RF switches, in which the insertion loss increases with frequency due to parasitic inductive effects <sup>1,8,15,17,19</sup>. The decreasing frequency dependency can be attributed to a parallel-plate on-state capacitance ( $C_{\rm on}$ ) in this nanoscale MIM structure, which is in parallel to the quasi-static  $R_{\rm on}$ . In switches made from bulk materials, this capacitance is negligible (compared to the inductance) due to the large device size. Quite fortuitously, in this nanoscale realization,  $C_{\rm on}$  provides the desirable benefit of reducing the insertion loss. The insertion loss of the hBN switch can be further reduced by increasing the d.c. compliance current (Fig. 2c and Supplementary Fig. 5a,b) that can be explained in terms of an increased number

NATURE ELECTRONICS ARTICLES

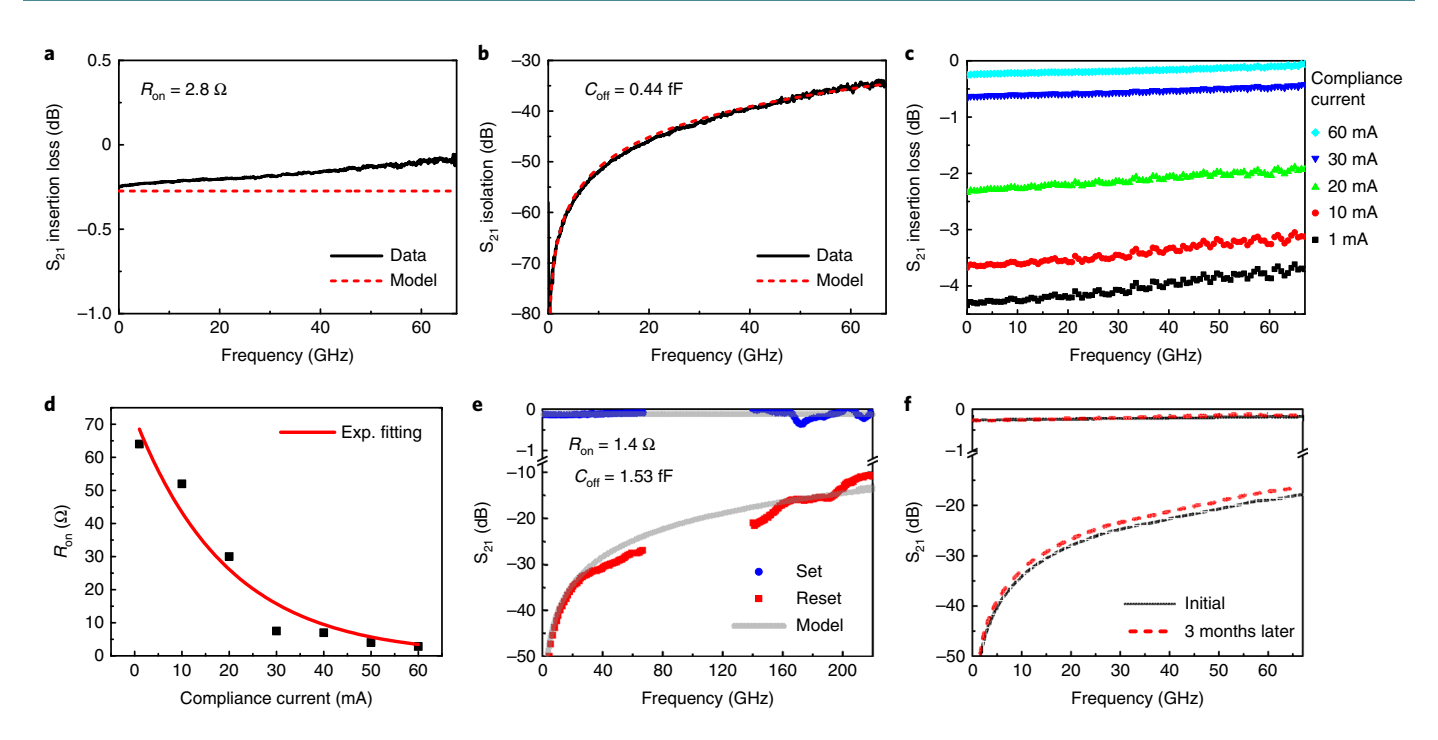


**Fig. 2** | **High-frequency performance of hBN non-volatile switch. a,b**, De-embedded experimental S-parameter  $S_{21}$  data in both the on (insertion loss) (a) and off (isolation) (b) states of RF switch. The device size is  $0.2 \times 0.15 \, \mu m^2$ . From the equivalent lumped element circuit model, the extracted  $R_{co}$  and  $C_{off}$  are  $2.8 \, \Omega$  and  $0.44 \, \text{fF}$ , respectively. The calculated  $F_{CO}$  is 129 THz. **c**, For the same device as for **a**, the d.c. switching compliance current can achieve tunable resistance and insertion loss. The upswing is attributed to the unique on-state capacitance that arises from the atomically thin vertical structure, which results in a non-negligible  $C_{cor}$ . **d**, The on-state resistance shows an exponentially decreasing dependency on the d.c. compliance current. **e**, Measured higher-frequency S-parameter ( $S_{21}$ ) data and model line into the terahertz range. The set and reset data are measured on  $0.5 \times 0.5 \, \mu m^2$  overlap area devices. **f**, S-parameter data show 3-months retention. The device size is  $0.5 \times 0.5 \, \mu m^2$ .

in the conductive filaments or widening of the filaments in the MIM structure  $^{13,20}$ . The corresponding  $R_{\rm on}$  dependence on the compliance current is shown in Fig. 2d and follows a  $R_{\rm on}=r_{\rm o}{\rm e}^{-x/b}$  relation with the fitting parameters  $r_{\rm o}=72\,\Omega$  and  $b=19.7\,{\rm mA}.$  Such variable (programmable) resistance states can be used in high-frequency device applications, such as non-volatile tunable resistors or attenuators.

Using a sophisticated probe station set-up, high-frequency measurements were extended to the terahertz range up to 220 GHz. The terahertz range refers to electromagnetic waves with frequencies between 100 GHz and 10 THz. The hBN device shows an insertion loss of less than 0.5 dB and isolation higher than 10 dB (Fig. 2e). This result represents a realization of a non-volatile electronic switch working in the terahertz range. The ripples observed in the extended frequency range from 140 to 220 GHz are largely due to standing waves that arise from impedance mismatch, which does not impact the main findings and can be improved by optimized transmission line matching to the experimental set-up. The aforementioned measurements took several months and hence provided an opportunity to evaluate the retention of the hBN switches, which is shown in Fig. 2f for a typical device and demonstrates good stability over 3 months at room temperature in air. It is expected that the retention is much longer<sup>28</sup>, and this matter is a topic of further research that warrants temperature-dependent accelerated testing.

# Data communication studies based on eye diagrams and BERs.

To highlight the potential offered by hBN switches, several data communication tests were conducted for  $f_c = 100 \, \text{GHz}$ , with numerous applications of backhauling for 5G and beyond. One of the key aspects of future high-bandwidth networks is the latency time, and hence systems have to be validated using real-time BER testing,

that is, without employing any power-hungry signal processing. In this context, amplitude modulation was chosen to demonstrate the capability of hBN switches to effectively route signals in the 100 GHz band. Figure 3a and Supplementary Fig. 6 present the experimental set-up used in this work, based on the photo-mixing of optical waves to efficiently generate high-speed modulated millimetre or terahertz wave signals<sup>29</sup>. In our experiments, we used data rates up to 8.5 Gbit s<sup>-1</sup>, according to the available bandwidth limit of the set-up (Fig. 3b). This 8.5 Gbit s<sup>-1</sup> data-rate limit is not due to the hBN overall bandwidth, which is far higher, according to the measured S-parameter frequency response.

To demonstrate the operation of the hBN device in an application scenario, the BER was recorded as a function of the input power  $(P_{in})$  (Fig. 3e). First, a reference measurement was conducted using a direct connection (through) between the probes and the BER performance was determined by the 100 GHz emission and reception circuits. Then, three sets of measurements were acquired on the same hBN switch (Fig. 3e): (1) first, the device was in the on state (blue curve), (2) then settled to the off state (red curve) and (3) lastly in the on state again (green curve). As can be seen, in the on state, the eye pattern is clear and the evolution of the BER values is the same as that using the reference (through), the power penalty being the small insertion loss of the hBN device over the frequency range of the modulated signal ( $100 \pm 8.5 \,\mathrm{GHz}$ ). For the off state, the isolation was 14dB, and the eye pattern almost closed, with a very low BER performance. Note that, due to the set-up limitation (available power at 100 GHz and envelope detector sensitivity), 15 dB was the highest measurable isolation to ensure enough power level to drive the BER tester. Higher isolations were achieved with other hBN devices, for which the BER was not measurable. After the validation at 8.5 Gbit s<sup>-1</sup>, lower data rates were tested (2 Gbit s<sup>-1</sup>)

ARTICLES NATURE ELECTRONICS

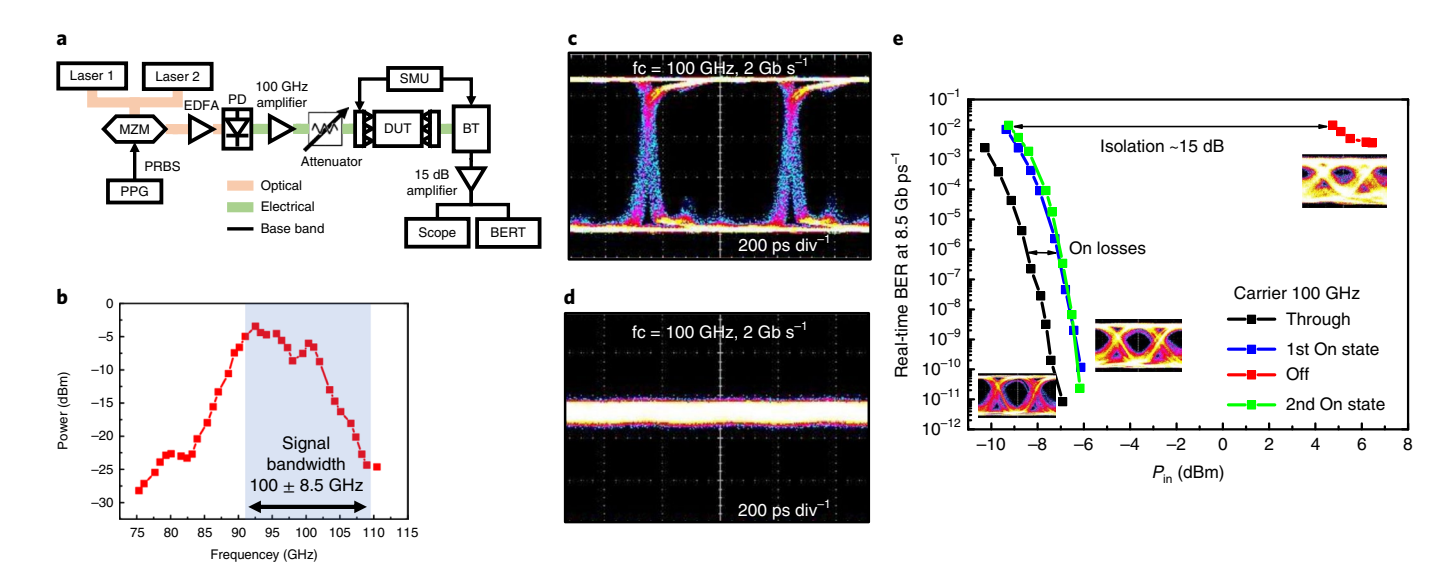


**Fig. 3 | Data communication performance. a**, Measurement set-up for eye diagrams and BERs. **b**, Frequency response of the measurement system. **c,d**, Switches at the on and off states show the opened (**c**) and closed (**d**) eye diagrams at  $f_c = 100 \,\text{GHz}$  and a bit rate of  $2 \,\text{Gbit s}^{-1}$ . **e**, BER measurements with different switch status. Insets: eye diagrams measured at  $f_c = 100 \,\text{GHz}$  with a bit rate of  $8.5 \,\text{Gbit s}^{-1}$  show similar on-state BER after a switching cycle. BERT, tester; div, division; DUT, device under test; EDFA, erbium-doped fibre amplifier; MZM, Mach-Zehnder modulator; PRBS, pseudo-random bit sequence; SMU, source measurement unit; BT, bias-tee; PD, photodiode; PPG, pulse pattern generator.

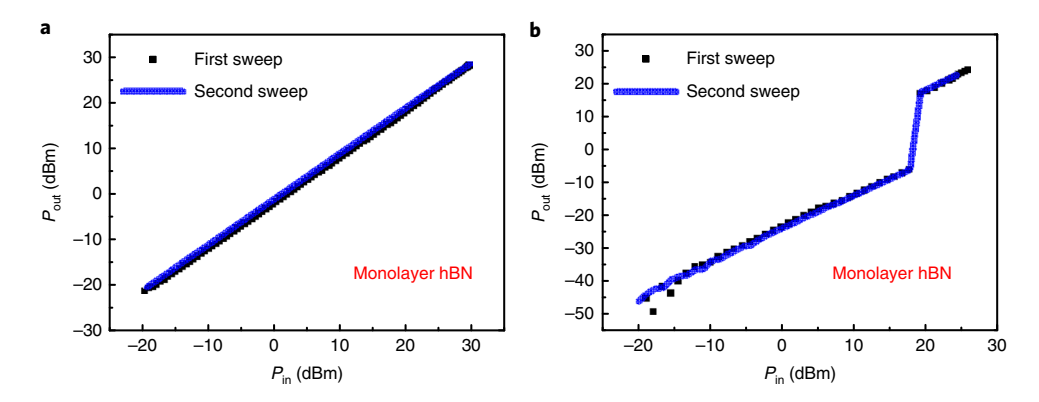


**Fig. 4 | Signal power handling of monolayer hBN RF switches. a,b**, Representative power handling measurement in the on (**a**) and off (**b**) states at 40 GHz for a monolayer hBN RF switch. The off state experiences self-switching at -20 dBm.

and an almost perfect eye pattern was obtained, with BER values below  $10^{-12}$  (Fig. 3c,d).

Beyond high-frequency characterization, the validation of any device for practical use requires demonstration in a realistic scenario. Therefore, a high-definition television data stream without any compression (1.5 Gbit s<sup>-1</sup>) was successfully encoded in the 100 GHz carrier, transmitted through the hBN device in the on state, decoded and displayed in real-time on a television (Supplementary Video 1 and Supplementary Note 2). When the device was electrically switched in the off state, the data transmission was interrupted and the television stream vanished.

RF power handling and self-switching. Power handling refers to the maximum power a switch can transmit in the on state while it retains high isolation in the off state. Figure 4 shows a typical on- and off-state power-handling measurement at 40 GHz in a monolayer hBN RF switch with a lateral area of  $0.5 \times 0.5 \,\mu\text{m}^2$  for RF  $P_{\text{in}}$  values from -20 to 30 dBm. In the on state, the output power increases linearly with  $P_{\text{in}}$  with negligible compression up to 30 dBm

(Fig. 4a). The insertion losses derived from power measurements are in strong agreement (within 0.1 dB) with the insertion losses derived from S-parameter measurements. In the off state, the output power presents high losses >20 dB, and a linear profile up to 19 dBm, and then the isolation is abruptly lost (Fig. 4b). This is due to 'self-switching' of the device from the off to the on state, which is attributed to self-bias from the high-power RF signal<sup>2</sup>. Accounting for feedline losses, this corresponds to a root-mean-square average voltage less than 2 V, which is reasonable compared with the d.c. switching voltage. Power-handling measurements at 18 GHz also confirmed the 40 GHz power data.

Notably, the hBN RF switch offers 10 dB more power handling compared with that of a  $MoS_2$  RF switch (Supplementary Table 1), and a factor-of-two higher power compared to memristive or  $VO_2$  phase-change switches. Also, the switch does not return to the high-resistance state when the power is turned off, which means that the device is non-volatile and indicates that, besides d.c. switching, the hBN device can also be switched remotely by wireless signals of sufficient amplitude. We validated this by remeasurement

NATURE ELECTRONICS ARTICLES

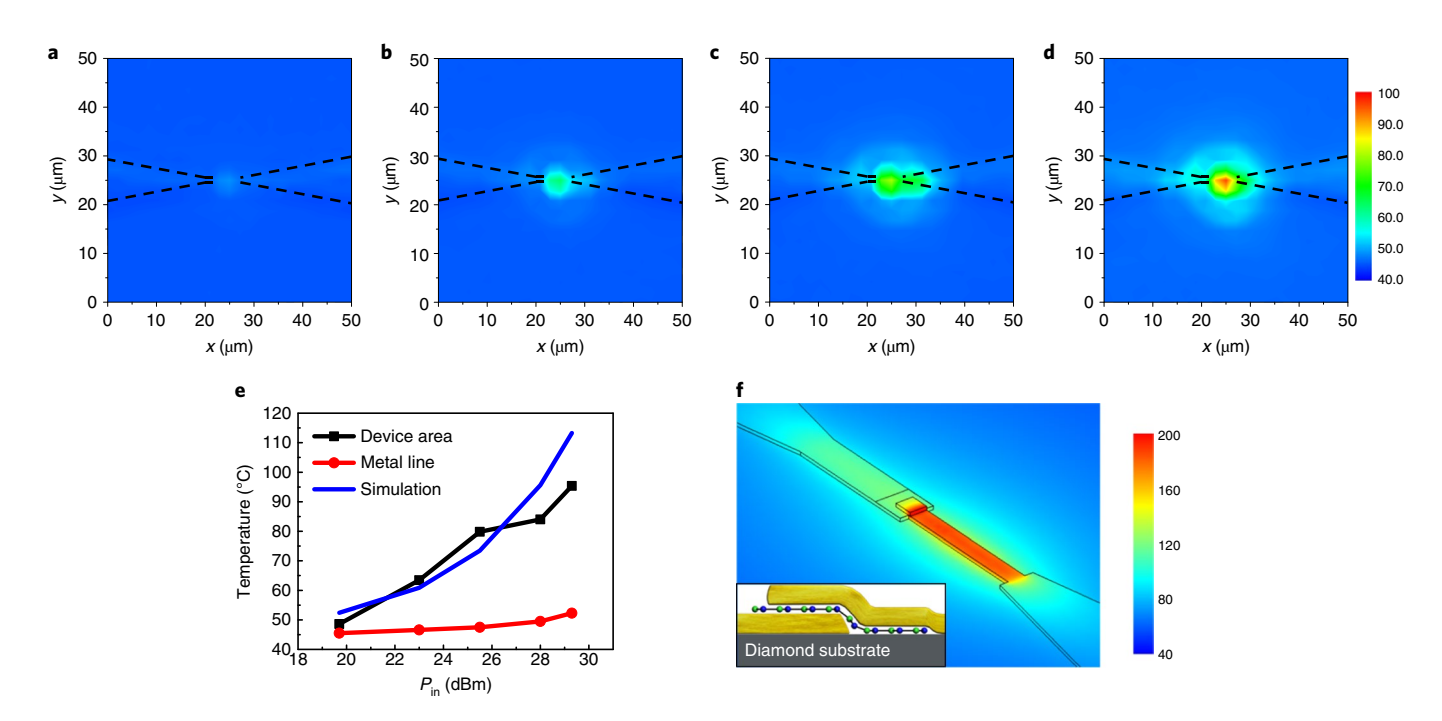


**Fig. 5 | Thermal mapping images and simulation. a-d**, Thermal mapping images (°C, colour scale) of hBN RF switch with RF  $P_{\rm in}$  values of 19.7 dBm (**a**), 23 dBm (**b**), 25.5 dBm (**c**) and 29.3 dBm (**d**). The dashed lines represent the edges of the Au signal lines that feed the RF power to the metal-hBN-metal junction. **e**, Experimentally measured temperature dependency versus  $P_{\rm in}$  at the device junction region and metal line. A COMSOL simulation in the junction area is included for electrothermal modelling purposes. The experimental data were collected by a  $2 \times 2 \,\mu\text{m}^2$  resolution infrared camera. **f**, COMSOL simulation using an a.c. and heat-transfer module shows a high temperature around the vertical MIM structure with a mesa configuration at a  $P_{\rm in}$  of 29.3 dBm. Inset: mesa structure of the current experimental device.

(Supplementary Fig. 7). As the hBN device was not damaged, it was switched from the on to the off state with a d.c. bias and then showed a similar self-switching when the RF power was applied again. Higher power handling requires a commensurately higher switching voltage, probably achievable by using few-layer hBN or using higher energy barrier metal electrodes, a matter for future research.

Electrothermal studies. We have shown that hBN switches with submicrometre dimensions can sustain a high power, about 20 and 30 dBm in the off and on states, respectively. At these power levels and given the small footprint of the switch, efficient heat dissipation becomes essential for reliable operation and to prevent device failure. In this regard, comprehensive electrothermal studies were conducted by combining infrared microscopy measurements and finite element simulations. Infrared microscopy is a non-invasive technique that can be used to map the absolute surface temperature of a sample.

As a fast and reliable calibration of an infrared camera requires the imaging of the sample at a well-known temperature, the substrate was kept at 45 °C during the whole experiment. The thermal mapping with spatial resolution  $\sim 2 \times 2 \, \mu \text{m}^2$  was achieved in situ during an actual high-power high-frequency switch operation. Figure 5a–d and Supplementary Fig. 8 show the thermal mapping of an hBN switch in the on state for  $P_{\text{in}}$ , which ranges from 19.7 to 29.3 dBm.

At approximatively 20 dBm, the temperature of the area that surrounds the junction started to rise above the substrate temperature of 45 °C. At this power, the high thermal conductivity of the diamond proved effective in limiting the temperature increase to only a few degrees. However, when the power was increased further, a hot spot centred at the junction area became clearly visible. For the maximum  $P_{\rm in}$  of 29.3 dBm, the temperature of the hot spot was sub-

stantially higher than that of the substrate, reaching 100 °C (Fig. 5d). As the junction area was only  $0.25\,\mu\text{m}^2$ , well below the pixel size of our camera, the measured value corresponds to the average temperature centred around the hot spot. The actual junction temperature was undoubtedly higher.

To shed further insight, electrothermal simulation of the same mesa device structure was conducted using the multiphysics software package COMSOL and showed comparable (for 2×2μm²) averaged temperatures to those of the thermal measurements (Fig. 5e,f). In addition, the simulation afforded a direct insight of the local hot-spot temperature at the junction, which was predicted to be approaching 250 °C at 30 dBm (Supplementary Fig. 9). A reliable switch operation, especially at a high signal power, is essential, especially for transmitter applications. As such, the validated simulation platform can be used to explore or optimize device structures for thermal management to minimize the temperature rise during operating conditions. The design space for a device design optimization includes mesa versus trench versus fully embedded device structures, choice and dimensions of metal electrodes, dielectric coating, number of monolayers and so on. Besides hBN, this simulation platform can be generalized to be applicable for the optimized design of emerging high-frequency switches made from transition metal dichalcogenides and metal oxides.

# **Conclusions**

We report here nanoscale non-volatile low-power analogue switches that are based on monolayer hBN and are suitable for applications in RF, 5G and terahertz communication and connectivity systems. The hBN high-frequency switches achieve a low insertion loss, high isolation (up to 220 GHz), and  $F_{\rm CO}$  values of about 129 THz due to its nanoscale vertical and lateral dimensions, which offer low resistance in the on state and low capacitance in the off state. For data communication systems, eye-diagram and BER measurements were

ARTICLES NATURE ELECTRONICS

conducted to evaluate the distortion, and revealed a good operation at a bit rate of  $8.5\,\mathrm{Gbit\,s^{-1}}$  and real-time video transmission. Signal power handling is of primary importance in wireless transmitter systems. Compared with  $\mathrm{MoS}_2$  switches, hBN switches offer good linearity and power handling up to  $\sim\!30\,\mathrm{dBm}$  in the on state, whereas off state power is limited by self-switching to  $\sim\!20\,\mathrm{dBm}$ . The relatively high-power handling is due to the larger bandgap and thermomechanical stability of hBN. Our work could lead to the development of a nanoscale energy-efficient high-frequency solid-state switch technology for the rapidly growing communication systems in the 5G band and beyond.

#### Methods

Device fabrication and characterization. The hBN RF switches were fabricated on 0.3-mm-thick polycrystalline CVD diamond substrate (from Element Six, thermal conductivity >1,000 W m<sup>-1</sup> K<sup>-1</sup>). The GSG device configuration was patterned by electron beam lithography. An electron-beam metal evaporation tool was used to create the ground pads and the BE, which consisted of 2-nm-thick chromium for the adhesion layer and 100-nm-thick Au. hBN atomic sheets were grown on copper foil using a standard CVD method<sup>30</sup> and then transferred to the fabricated BE using a poly(methyl methacrylate)-assisted wet-transfer method. Then, electron beam lithography and a plasma etching process were used to define the active region of the hBN film. Lastly, the TE was patterned and deposited by using the same fabrication process as used for the BE. The d.c. measurements were conducted on a Formfactor probe station with a Keysight 4156 semiconductor parameter analyser under ambient conditions. We prepared an array of devices, and 18 devices worked out of 36 devices. Therefore, the yield was 50%. We expect the yield to increase further with engineering optimization of the material transfer process, device microfabrication and electrostatic discharge handling of the fabricated samples. The Renishaw in-Via system with a 532-nm-wavelength source was used for monolayer hBN Raman spectroscopy. Atomic force microscopy images were collected using a Vecco Nanoscope with tapping mode.

RF measurements. RF measurements were conducted using a Keysight E5270 source meter unit and various VNAs with Formfactor Infinity GSG probes. R&S ZVA24 with a frequency converter, a ZVA110 and an Agilent E8361A VNA were used to cover 0.1-110 GHz and 140-220 GHz bands. The sample was placed on top of an absorber (from Formfactor) to avoid coupling to the sample holder. The source RF power was set to  $-16 \, \mathrm{dBm}$ , which is in the small signal range for S-parameter measurements to avoid non-linear effects. For on-wafer calibration, SOLT calibration was used for the 67 GHz set-up and LRRM calibration was used for the 220 GHz set-up, and calibrations were carried out using a Cascade calibration kit and WinCal software (Formfactor Inc.) to obtain precise results and to remove the parasitic effects of impedances that arise from the cables and probe station<sup>31</sup>. The S parameters were measured in the on and off states. As the hBN switch device has a non-volatile resistive switching phenomenon, we applied a forward and reverse d.c. bias to turn on and off the switching device, respectively. Therefore, we use the forward d.c. bias (set voltage) to switch the device from the off state to the on state at first. Then we measured the S parameter of the on state using a VNA without a d.c. bias. Afterwards, we applied the reverse d.c. bias (reset voltage) to turn off the device. Similarly, we measured the S parameter of the device at the off state using a VNA without d.c. bias. An open-short de-embedding process was used to remove the pad and interconnect resistances. RF power handling was measured using a Keysight PNA-X VNA with Formfactor Z probes. A continuous-wave signal with power levels from -20 to +30 dBm at 40 GHz was applied to evaluate the power-handling capability in both the on and off states by measuring a/b parameters and power inputs and outputs at the device.

Data communication testing. Two 1,550 nm lasers, separated by 0.8 nm (this separation corresponds to  $100\,\mathrm{GHz}$ ), were amplitude modulated using a MZM and a pseudo-random bit sequence with a  $2^9-1$  length. The modulated optical signals were used to feed a 100 GHz photodiode, which generated a modulated 100 GHz electrical signal, thanks to the photo-mixing downconversion inside the photodiode. This 100 GHz signal was then amplified, and a variable attenuator used to accurately control the power level at the input port of the device under test. After the propagation across the device, the 100 GHz signal was detected by a Schottky barrier diode, used as an envelope detector, and subsequently amplified by a 15-dB-gain stage. The latter was connected to a buffer amplifier (Hittite HMC866) used to reach the required signal level to drive the bit error rate tester. All the adjustments (MZM driving voltage, threshold and clock  $\,$ recovery) were done using the wafer-level reference transmission line. In these conditions, the obtained absolute BER values are directly related to the intrinsic performances of the 100 GHz set-up (photodiode, amplifier and Schottky diode) only. Then, the BER were measured with the hBN devices, in several on and off states. With this approach, the BER performance can thus be compared with the reference transmission line to highlight the capacity of the device to handle

the 100-GHz-modulated signals. In these conditions, the variation of the power required to reach a constant BER value corresponds to the power penalty, shown by on losses in Fig. 3e.

**Thermal mapping.** In the thermal mapping experiment, an infrared camera (MWIR-512 from Quantum Focus) was used with a  $\times 12$  objective. The spatial resolution was  $2\times 2\,\mu\text{m}^2$  (which corresponds to one pixel in the thermal map). The sample was kept at 45 °C by controlling the sample-holder temperature. As the CVD diamond substrate and hBN film were infrared transparent, only the coplanar waveguide metal electrodes were reflected in the infrared image. The infrared camera was calibrated using the emission recorded from the sample without any applied RF bias. The calibration and the thermal mapping measurements were performed with software from Quantum Focus.

As the infrared microscope is mounted on a microwave probe station, the temperature of a device under high-frequency operation can be mapped in situ. The continuous-wave signal from a Keysight PNA-X VNA at 18 GHz was amplified and sent through the device via Formfactor Z coplanar probes; two power meters (HP438A) and two directional couplers were used to precisely determine the input and output power at the device plane while recording the temperature distribution.

**Reporting summary.** Further information on research design is available in the Nature Research Reporting Summary linked to this article.

#### Data availability

The data that support the plots within this paper and other finding of this study are available from the corresponding author upon reasonable request.

Received: 27 November 2019; Accepted: 20 April 2020; Published online: 25 May 2020

#### References

- Pi, S., Ghadiri-Sadrabadi, M., Bardin, J. C. & Xia, Q. Nanoscale memristive radiofrequency switches. Nat. Commun. 6, 7519 (2015).
- Lee, J.-L., Zych, D., Reese, E. & Drury, D. M. Monolithic 2–18 GHz low loss, on-chip biased PIN diode switches. *IEEE Trans. Microw. Theory Tech.* 43, 250–256 (1995).
- Larson, L. E. Integrated circuit technology options for RFICs—present status and future directions. IEEE J. Solid-State Circuits 33, 387–399 (1998).
- Brown, E. R. RF-MEMS switches for reconfigurable integrated circuits. IEEE Trans. Microw. Theory Tech. 46, 1868–1880 (1998).
- Yao, J. J. RF MEMS from a device perspective. J. Micromech. Microeng. 10, R9 (2000).
- Li, Q., Zhang, Y. P., Yeo, K. S. & Lim, W. M. 16.6-and 28-GHz fully integrated CMOS RF switches with improved body floating. *IEEE Trans. Microw. Theory Tech.* 56, 339–345 (2008).
- Stefanini, R., Chatras, M., Blondy, P. & Rebeiz, G. M. Miniature MEMS switches for RF applications. J. Microelectromech. Syst. 20, 1324–1335 (2011).
- 8. Patel, C. D. & Rebeiz, G. M. A compact RF MEMS metal-contact switch and switching networks. *IEEE Microw. Wirel. Compon. Lett.* 22, 642–644 (2012).
- Wang, M. & Rais-Zadeh, M. Development and evaluation of germanium telluride phase change material based ohmic switches for RF applications. J. Micromech. Microeng. 27, 013001 (2017).
- El-Hinnawy, N. et al. Origin and optimization of RF power handling limitations in inline phase-change switches. *IEEE Trans. Electron Devices* 64, 3934–3942 (2017).
- 11. Madan, H. et al. in 2015 IEEE International Electron Devices Meeting (IEDM) 9.3.1–9.3.4 (IEEE, 2015).
- Olsson, R. H., Bunch, K. & Gordon, C. in 2016 IEEE Compound Semiconductor Integrated Circuit Symposium (CSICS) 1–4 IEEE (2016).
- 13. Wong, H. S. P. et al. Metal-oxide RRAM. Proc. IEEE 100, 1951-1970 (2012).
- 14. Wouters, D. J., Waser, R. & Wuttig, M. Phase-change and redox-based resistive switching memories. *Proc. IEEE* **103**, 1274–1288 (2015).
- Field, M. et al. in Proc. SPIE 9479 Open Architecture/Open Business Model Net-Centric Systems and Defense Transformation 2015 947908 (International Society for Optics and Photonics, 2015).
- Ge, R. et al. Atomristor: nonvolatile resistance switching in atomic sheets of transition metal dichalcogenides. *Nano Lett.* 18, 434–441 (2018).
- Kim, M. et al. Zero-static power radio-frequency switches based on MoS<sub>2</sub> atomristors. Nat. Commun. 9, 2524 (2018).
- Chappell, W. J., Hancock, T. M. & Olsson, R. H. in 2018 IEEE/MTT-S International Microwave Symposium—IMS) 829–831 (IEEE, 2018).
- Léon, A. et al. RF power-handling performance for direct actuation of germanium telluride switches. *IEEE Trans. Microw. Theory Tech.* 68, 60–73 (2020).
- Wu, X. et al. Thinnest nonvolatile memory based on monolayer h-BN. Adv. Mater. 31, 1806790 (2019).
- Shi, Y. et al. Electronic synapses made of layered two-dimensional materials. Nat. Electron. 1, 458 (2018).

NATURE ELECTRONICS ARTICLES

- Zhao, H. et al. Atomically thin femtojoule memristive device. Adv. Mater. 29, 1703232 (2017).
- Zhang, C. J. et al. Key technology for 5G new radio. IEEE Commun. Mag. 56, 10–11 (2018).
- 24. Ge, R. et al. in 2018 IEEE International Electron Devices Meeting (IEDM) 22.6.1–22.6.4 (IEEE, 2018).
- 25. Lee, Y. H. et al. Synthesis and transfer of single-layer transition metal disulfides on diverse surfaces. *Nano Lett.* **13**, 1852–1857 (2013).
- Cha, J., Cha, J. & Lee, S. Uncertainty analysis of two-step and three-step methods for deembedding on-wafer RF transistor measurements. *IEEE Trans. Electron Devices* 55, 2195–2201 (2008).
- Liu, A.-Q. RF MEMS Switches and Integrated Switching Circuits (Springer Science & Business Media, 2010).
- 28. Li, L. H. & Chen, Y. Atomically thin boron nitride: unique properties and applications. *Adv. Funct. Mater.* **26**, 2594–2608 (2016).
- Nagatsuma, T., Ducournau, G. & Renaud, C. C. Advances in terahertz communications accelerated by photonics. *Nat. Photon.* 10, 371–379 (2016).
- 30. Kim, K. K. et al. Synthesis of monolayer hexagonal boron nitride on Cu foil using chemical vapor deposition. *Nano Lett.* **12**, 161–166 (2012).
- 31. Application Note on Wafer Vector Network Analyzer Calibration and Measurements (Cascade Microtech, 1997).

### **Acknowledgements**

This work was supported in part by the Office of Naval Research grant N00014-20-1-2104, the National Science Foundation (NSF) grant no. 1809017 and Engineering Research Center Cooperative Agreement no. EEC-1160494. D.A. acknowledges the Presidential Early Career Award for Scientists and Engineers (PECASE) through the Army Research Office Award no. W911NF-16-1-0277. The fabrication was partly done at the Texas Nanofabrication Facility supported by NSF grant NNCI-1542159. hBN

samples were kindly provided by Grolltex, Inc. The characterization part of this work was partly supported by the European Union's Horizon 2020 research and innovation programme under the phase of the Graphene Flagship GrapheneCore2 785219, by an ANR TERASONIC grant (17-CE24) and by the CPER Photonics for Society, the Hauts-de-France regional council and the TERIL-WAVES project (I-Site ULNE and MEL).

#### **Author contributions**

M.K. performed material transfer, characterization, device fabrication, low-frequency measurements and COMSOL simulation. E.P. contributed to high frequency, high power and thermal measurements. G.D. and E.P. conducted eye diagrams and BER measurements. R.G., X.W. and J.C.L. contributed to the development of hBN as a memory device. M.K., E.P. and D.A. analysed the electrical data and characteristics. All the authors contributed to the article based on the draft written by M.K., E.P. and D.A. H.H. and D.A. initiated and supervised the collaborative research.

## **Competing interests**

The authors declare no competing interests.

#### Additional information

**Supplementary information** is available for this paper at https://doi.org/10.1038/s41928-020-0416-x.

Correspondence and requests for materials should be addressed to D.A.

Reprints and permissions information is available at www.nature.com/reprints.

**Publisher's note** Springer Nature remains neutral with regard to jurisdictional claims in published maps and institutional affiliations.

 $\ensuremath{\texttt{©}}$  The Author(s), under exclusive licence to Springer Nature Limited 2020